HHS Public Access

Author manuscript

*J Immunol*. Author manuscript; available in PMC 2022 April 15.

Published in final edited form as:

*J Immunol*. 2021 April 15; 206(8): 1890–1900. doi:10.4049/jimmunol.2001016.

# Loss of Mitochondrial Protease CLPP Activates Type I IFN Responses through the Mitochondrial DNA–cGAS–STING Signaling Axis

**Sylvia Torres-Odio**[*], **Yuanjiu Lei**[*], **Suzana Gispert**[†], **Antonia Maletzko**[†], **Jana Key**[†], **Saeed S. Menissy**[*], **Ilka Wittig**[‡], **Georg Auburger**[†], **A. Phillip West**[*,#]

[*]Department of Microbial Pathogenesis and Immunology, College of Medicine, Texas A&M University Health Science Center, Bryan, TX 77807, USA

[†]Experimental Neurology, Faculty of Medicine, Goethe University, 60590 Frankfurt am Main, Germany

[‡]Functional Proteomics, Faculty of Medicine, Goethe University, 60590 Frankfurt am Main, Germany

## Abstract

Caseinolytic mitochondrial matrix peptidase proteolytic subunit, CLPP, is a serine protease that degrades damaged or misfolded mitochondrial proteins. CLPP null mice exhibit growth retardation, deafness, and sterility, resembling human Perrault syndrome (PS), but also display immune system alterations. However, the molecular mechanisms and signaling pathways underlying immunological changes in CLPP null mice remain unclear. Here we report the steady state activation of type I interferon (IFN-I) signaling and antiviral gene expression in CLPP deficient cells and tissues, resulting in marked resistance to RNA and DNA virus infection. Depletion of the cyclic GMP-AMP (cGAS)-Stimulator of Interferon Genes (STING) DNA sensing pathway reduces steady state IFN-I signaling and abrogates the broad antiviral phenotype of CLPP null cells. Moreover, we report that CLPP deficiency leads to mitochondrial DNA (mtDNA) instability and packaging alterations. Pharmacological and genetic approaches to deplete mtDNA or inhibit cytosolic release markedly reduce antiviral gene expression, implicating mtDNA stress as the driver of IFN-I signaling in CLPP null mice. Our work places the cGAS-STING-IFN-I innate immune pathway downstream of CLPP and may have implications for understanding PS and other human diseases involving CLPP dysregulation.

## INTRODUCTION

Mitochondrial proteases are key modulators of several mitochondrial functions, including the maturation of proteins, maintenance of protein quality control, control of mitochondrial gene expression and biogenesis, mitophagy, and apoptosis (1). CLPP, caseinolytic mitochondrial matrix peptidase proteolytic subunit, is a highly conserved, processive serine protease located in the mitochondrial matrix. CLPP is the protease component of the CLPXP

[#]Address correspondence to Dr. A. Phillip West, 8447 Riverside Parkway, MREB1 3012, Bryan, TX 77807. awest@tamu.edu. Phone: (979) 436-0870.

complex that cleaves peptides and various proteins in an ATP-dependent process, together with chaperone and ATPase CLPX (2). While prokaryotic ClpXP has been extensively studied, the role and function of CLPXP in mitochondria remain less clear, and there is limited information regarding its specific substrates (3). Studies in *C. elegans* have implicated CLPXP as a key component of the mitochondrial unfolded protein response ($UPR^{mt}$), and downstream signaling and transcriptional responses of the $UPR^{mt}$ are attenuated in worms lacking CLPP activity (4, 5). Mammalian CLPP is involved in pleiotropic cellular functions such as myoblast differentiation, cell proliferation, and mitoribosome assembly, which controls the rate of mitochondrial protein synthesis (6, 7). Moreover, CLPP has recently been implicated in cancer, and hyperactivating CLPP was shown to alter mitochondrial function and selectively kill some cancer cells (8). Thus, drugs targeting CLPP are new candidates for cancer therapy (9).

Studies performed in CLPP null mice (CLPP-KO) highlight the physiological and pathological relevance of this model to the human disorder known as Perrault syndrome (PS). CLPP-KO mice display profound phenotypic changes characterized by growth retardation, deafness, and premature sterility, despite exhibiting only mild mitochondrial bioenergetic deficits (10). Similar phenotypes are also observed in PS, where the genetic component involves autosomal recessive mutations in CLPP and other nuclear DNA-encoded mitochondrial proteins (11). Other phenotypes of this mouse include insulin resistance and protection from diet-induced obesity (12), accelerated depletion of ovarian follicular reserve (13), and impairment of adaptive thermogenesis due to a decline in brown adipocytes (14).

Eukaryotic mitochondria maintain prokaryotic features, including a double-stranded circular DNA genome, inner membrane cardiolipin, and N-formylated proteins, which act as potent triggers of innate immune sensors when released from mitochondria into the cytosol or extracellular space. The release and accumulation of these so-called mitochondrial damage-associated molecular patterns (DAMPs) are increasingly implicated in the inflammatory pathology of human disorders including autoimmunity, neurodegenerative diseases, and cancer (15–17). Our prior work identified antiviral gene signatures in CLPP-KO mice consistent with steady state activation of innate immunity (10, 18). However, the mitochondrial molecular mechanisms and innate immune signaling pathways underlying activation of antiviral signatures in CLPP-KO mice remain uncharacterized, and the biological significance of this phenotype is unclear.

Here we show that enhanced antiviral gene expression in CLPP-KO mice is triggered by mtDNA release and mediated by the cGAS-STING DNA sensing pathway. Deletion of STING or the interferon α/β receptor (IFNAR) in CLPP-KO MEFs ablates steady state expression of broadly antiviral ISGs and reduces the potent antiviral phenotypes observed during RNA and DNA virus infection. These findings shed light on a new mitochondrial pathway upstream of cGAS and STING, link mitochondrial proteostasis to mtDNA genome maintenance, and may have important implications for understanding mitochondrial-innate immune crosstalk in the context of human health and disease.

# MATERIALS AND METHODS

## Mouse Strains

Embryonal stem cell line IST13563G11 (line G), with heterozygous GeneTrap insertions at *Clpp* intron 2, was re-derived at the Texas Institute for Genomic Medicine (TIGM) on a C57BL/6N background. Heterozygous breeders were mated to generate *Clpp*-null (CLPP-KO) mutant and littermate WT control offspring. *Sting*$^{gt/gt}$ (C57BL/6J-*Sting1*$^{gt}$/J, strain 017537) and *Ifnar*$^{-/-}$ (B6(Cg)-*Ifnar1*$^{tm1.2Ees}$/J, strain 028288) were obtained from the Jackson Laboratory. CLPP heterozygous mutant mice were crossed with *Sting*$^{gt/gt}$ and *Ifnar*$^{-/-}$ for several generations to obtain double KO mice on a C57BL/6NJ mixed background. All animal experiments were conducted in compliance with the guidelines established by the Texas A&M University Institutional Animal Care and Use Committee (IACUC).

## Cell Culture

Primary wild-type, CLPP-KO, STING$^{gt/gt}$, IFNAR$^{-/-}$ (IFNAR-KO), CLPP-KO/STING$^{gt/gt}$ and CLPP-KO/IFNAR-KO MEFs were generated from E12.5–14.5 embryos. Cells were maintained in DMEM (D5756–500ML, Sigma) supplemented with 10% FBS (VWR), and sub-cultured for no more than five passages before experiments. Transfection of MEFs with siRNA was performed with Lipofectamine-RNAi Max (13778–150, Invitrogen) in Opti-MEM media (11058021, ThermoFisher Scientific) and the following siRNAs were used at a final concentration of 25nM: sicGAS (MMC.RNAI.N173386.12.1 IDT), siRNA mPolg2 (NM_015810 Sigma-Aldrich), siMfn1 (NM_024200 Sigma-Aldrich), siDrp1 (MMC.RNAI.N152816.12.1), siClpX (MMC.RNAI.N011802.12.2 IDT) and siRNA NTC (Negative Control DsiRNA, 51-01-14-03, IDT) according to manufacturer's instructions. Cells were harvested for RNA or protein between 48–72hrs later. For Rig-I/MDA5 challenge, cells were transfected with Poly(I:C) (P1530, SIGMA) complexed in polyethylenimine (PEI, 43896, Alfa Aesar) in Opti-MEM media. For LPS, cells were treated with LPS (LPS-B5 Ultrapure, InvivoGen tlrl-pb5lps) at 1μg/ml and harvested for RNA 4hrs later. For mtDNA depletion, ddC (D5782, SIGMA) was resuspended in PBS, added to MEFs at a final concentration of 150μM and refreshed every 48hrs for 4 days. For Chloramphenicol (CAM) treatment, cells were treated with CAM (R4408, SIGMA) at different concentrations (50–200μM) and harvested for protein between 24–48hrs later. For VBIT-4 treatment, VBIT-4 (HY-129122, MedChem Express) was resuspended in DMSO at 10mM and added to the media at a final concentration of 10μM during 48hrs while control cells were treated with DMSO. For VBIT-4 treatment plus challenge, cells were treated with VBIT-4 and 6hrs before the 48hrs harvesting time. mIFNβ (8234-MB-010/CF, R&D) was added to the cells at a final concentration of 1ng/ml. All cells were harvested 48hrs after challenge for RNA analysis. To generate CLPP knockdown human foreskin fibroblasts (HFF-1), MISSION shRNA Lentiviral Transduction Particles against human CLPP (TRCN0000291174) or eGFP (RHS4459) were purchased from Sigma-Aldrich and Horizon Discovery respectively. HFF-1 were transduced with the shRNA encoding lentivirus stocks in the presence of polybrene (8μg/ml) and stably selected with puromycin.

### Viral stocks and infections

VSV-G/GFP and HSV1/GFP were maintained as described previously (19, 20). MEFs were plated in 12-well plates at $7\times10^4$ cells/well, 16hrs before infection in DMEM+10% FBS. The next morning, virus stocks were diluted at indicated MOIs in serum-free DMEM (D5756–500ML, Sigma). 300μl serum-free media containing virus (or DMEM alone for the control wells) was gently added to wells. Plates were incubated at 37°C 5% $CO_2$ and rocked gently every 15 min for 1hr, after which the supernatant was removed, bleached, and discarded. Then, 0.5 mL of fresh DMEM+10% FBS was added to each well, and the cells were allowed to incubate for the duration of the experiment. At the indicated times post infection, supernatant was collected and cleared by centrifugation at 6,000 rpm, 4°C, then kept at −80°C until further processing. Cells were then fixed and stained for microscopy or lysed in RNA Lysis buffer. For plaque assay: BHK-1 or Vero cells were plated in 6-well plates at 95% confluency in 3% Methylcellulose containing DMEM media. Next, different dilutions of supernatant from VSV or HSV1 infected MEFs were added to the cells and incubated until plaques were visible, between 24–72hrs. Plaques were stained with Cresyl Violet and counted with Image J software.

### Immunofluorescence microscopy

Cells were grown on 12mm or 18mm coverslips and treated or infected as described. After washing in PBS, cells were fixed with 4% paraformaldehyde for 20 min, permeabilized with 0.1% Triton X-100 in PBS for 5 min, blocked with PBS containing 10% FBS for 30 min, stained with primary antibodies for 60 min, and stained with secondary antibodies for 60 min. Cells were washed with PBS between each step. Coverslips were mounted with Prolong Gold anti-fade reagent containing DAPI (Molecular Probes). For viral infections, viral GFP fluorescence images were captured using the LionHeart FX fluorescent microscope at 20X and tiling images at 2×2. For mtDNA nucleoid staining, a 60X oil-immersed objective was used and images were taken with a Confocal Laser Scanning Microscope (Olympus FV3000). Images were processed in Image J software. Nucleoid area quantification was performed largely as described (21). Briefly, approximately 6–8 unique fields of view from 5 distinct confocal images (of each genotyping at each treatment) comprising between 200–400 nucleoids, were captured at random. After incorporating scale information obtained from the FV3000 software, images were made binary and the area of each nucleoid was determined using the ‘Analyze Particles’ feature of ImageJ. Nucleoids were binned into the three size cut-offs (<200nm$^2$; between 200–450nm$^2$; and >450nm$^2$), and the percentage of nucleoids falling within each category was plotted.

### Quantitative PCR

To measure relative gene expression by qRT-PCR, total cellular RNA was isolated using the Quick-RNA Micro Prep Kit (R1051, Zymo Research). Approximately 250–500ng RNA was normalized across samples and cDNA was generated using the qScript cDNA Synthesis Kit (101414–098, VWR). cDNA was then subjected to qPCR using PerfecTa SYBR Green FastMix (84069, Quantabio) and primers as indicated in Table 1. Three technical replicates were performed for each biological sample, and expression values of each replicate were normalized against Rp137 using the $2^{-\Delta ddct}$ method. For relative expression (fold), control

samples were centered at 1; for relative expression (%), control samples were centered at 100%. Mitochondrial DNA abundance analysis was performed as described above using primers specific to mtDNA regions and normalized against nuclear *Tert*.

## Proteomics

CLPP-KO MEF and their matching controls (n=3) were analyzed by quantitative mass spectrometry essentially as described in (22). Mass spectrometry data were analyzed by MaxQuant (1.5.3.30) (23) using a mouse proteome Uniprot database (Download 2/2016) and a false discovery rate (FDR) less than 1%. For quantification, proteins were quality filtered according to a minimum of three valid values in one group (n=3) using Perseus software (v. 1.5.2.6). All missing values from this reduced matrix were replaced by background value from normal distribution. For statistical comparison, students t-tests were used. The mass spectrometry proteomics data have been deposited to the ProteomeXchange Consortium (http://proteomecentral.proteomexchange.org) via the PRIDE partner repository with the dataset identifier PXD023677.

## Subcellular fractionation

Cellular fractionation was performed largely as described (24). In brief, cells were divided into two aliquots, and one aliquot (10%) was resuspended in 50μl of 1% SDS lysis buffer, boiled for 5 min, sonicated for 1 min and saved as whole-cell lysate (WCL). The second equal aliquot (90%) was resuspended in 400μl extraction buffer containing 10mM HEPES, 10mM KCl, 1.5mM $MgCl_2$, 0.34 M sucrose, 10% glycerol, 0.2% NP-40, pH 7–7.6, and protease inhibitors. The homogenates were incubated on ice for 10 min with occasional vortexing, centrifuged at 6,500g for 5 min three times, and the supernatant was saved as the post-nuclear fraction. The nuclei were then washed for 1 min on ice in extraction buffer and centrifuged at 6,500*g* for 5 min at 4 °C twice, resuspended in 150μl of 1% SDS lysis buffer, boiled at 95 °C for 5 min and sonicated for 1 min. After a high speed 20,000g spin to pellet sheared DNA, the supernatant was saved as the nuclear fraction.

## Immunoblotting

Proteins from either homogenized tissue (<50mg) or cells ($<1\times10^7$) were lysed in 1% NP40 buffer, and spun down at 15,000 rpm for 10 min at 4°C. The supernatant was collected as protein lysate and quantified with micro-BCA assay (23235, Proteintech). Between 20–30μg of protein were separated on 10–20% polyacrylamide gradient gels, then transferred onto PVDF membranes at 100V for 1hr. Membranes were dried for 30 min and incubated with primary antibodies (Table 2) overnight at 4°C. Membranes were washed with 1X PBS for 30 min and incubated with HRP-conjugated secondary antibodies for 1hr. Membranes were washed with PBS for 1 hr before developing with Millipore Luminata Crescendo HRP Substrate (WBWR0500).

## EchoMRI

Body composition analysis on live mice was completed using the EchoMRI™−100H at the Rodent Preclinical Phenotyping Core at Texas A&M University. This analyzer delivers

precise body composition measurements of fat, lean, free water, and total water masses in live animals weighing up to 100g.

### Statistical analyses

Error bars displayed throughout the manuscript represent the mean +/− s.e.m. unless otherwise indicated and were calculated from triplicate or quadruplicate technical replicates of each biological sample. Sample sizes were chosen by standard methods to ensure adequate power, and no randomization or blinding was used for animal studies. No statistical method was used to predetermine sample size. Statistical analysis was determined using GraphPad software and statistics tests include: unpaired Student's t-tests, ordinary one-way ANOVA and two-way ANOVA with Tukey's *post-hoc*. Significance was stablished as *p<0.05; **p<0.01; ***p<0.001; ****p<0.0001; or not significant (ns) when p>0.05. Data shown are representative of 2–3 independent experiments (unless otherwise specified) including microscopy images, Western blots, and viral challenges.

## RESULTS

### CLPP deficiency leads to steady state ISG expression and an antiviral signature in cells and tissues.

We first expanded upon our prior findings that revealed increased steady state expression of antiviral genes in CLPP deficient tissues (10). Using Ingenuity Pathway Analysis (IPA) software, we observed that predicted upstream regulators of the antiviral gene signature in CLPP-KO tissues included factors governing IFN-I signaling (*Irf7*, *Irf3* and *Stat1*), IFNα, and IFNAR (Fig. S1A). Among the list of upregulated IRF7 and STAT1 target genes, we identified canonical ISGs such as *Usp18*, *Ifit1b*, *Ifi44*, and *Rtp4* (Fig. S1B). Individual analyses of heart and liver tissues from 3–5-month-old mice revealed a significant enhancement of ISGs at the protein level in both the liver and heart of CLPP-KO mice (Fig. S1C–D).

To better characterize this ISG response, we used mouse embryonic fibroblasts (MEFs) and human foreskin fibroblasts deficient in CLPP. Expression profiles of CLPP-KO MEFs revealed an enrichment of ISGs and antiviral signaling factors at both the RNA and protein level (Fig. 1A–C). Among the set of overexpressed ISGs, we observed those involved in direct antiviral activity (VIPERIN/Rsad2, IFIT1, IFIT3); regulators of antiviral and IFN-I signaling (USP18, STAT1, STAT2); as well as RNA and DNA sensors (RIG-I, MDA5, and ZBP1). Global proteome profiling revealed that greater than 60 percent of the most differentially expressed proteins in CLPP-KO MEFs were ISGs (Fig. 1C). Consistent with enhanced IFN-I responses and ISG expression, CLPP-KO MEFs showed elevated levels of transcription factors IRF7, STAT1 and STAT2 in whole cell and nuclear fractions compared to WT cells (Fig. 1D). Similarly, CLPP-KO cells showed higher transcript levels of *Ifnb1*, but no significant differences in interferon alpha gene expression (*Ifna1*, *Ifn14*, *Ifna5*) (Fig 1E).

Transfection of CLPP-KO MEFs with poly(I:C), a dsRNA analog agonist of the cytosolic RNA helicase MDA5, or challenge with LPS, a TLR4 ligand, revealed elevated ISG

expression compared to WT, which indicates potentiation/priming of antiviral signaling pathways downstream of both cytosolic and membrane-bound pattern recognition receptors (Fig. 1F). To assess if this heightened ISG response was only observed in mouse cells, we transduced human foreskin fibroblasts with short hairpin RNAs targeting CLPP (shCLPP) or EGFP as a control (shEGFP). Similar to our findings in MEFs and murine tissues, reduction of CLPP in human fibroblasts led to the steady state upregulation of antiviral ISGs at the protein level, including IFIT2, IFITM1, RIG-I, STAT1 and others (Fig. 1G).

## STING and IFNAR mediate the steady state ISG and antiviral signature observed in CLPP deficient cells and tissues.

Recent work has revealed that the release of mitochondrial nucleic acid DAMPs into the cytosol is a potent trigger of DNA and RNA sensors of the innate immune system (21, 25, 26). To next pinpoint downstream sensors mediating the antiviral response in CLPP-KO cells, we transiently knocked down the DNA sensor cGAS or the cytosolic RNA adaptor MAVS and quantified ISG responses in MEFs. Downregulation of cGAS profoundly diminished the ISG response in CLPP-KO MEFs (Fig. 2A) while MAVS depletion did not (Fig. S2A), implicating the cytosolic DNA sensing machinery as the main trigger of ISGs in CLPP deficient cells. Using a parallel approach to bypass any off-target and immune stimulatory effects of transient siRNA transfection, we crossed CLPP heterozygous mutant mice with *Sting*$^{gt/gt}$ and *Ifnar*$^{-/-}$ strains to generate CLPP-KO/STING$^{gt/gt}$ and CLPP-KO/IFNAR-KO mice, respectively, and assessed the antiviral response in MEFs and tissues. Consistent with our siRNA data implicating the cGAS pathway, the relative expression of ISGs *Usp18*, *Isg15*, *and Cxcl10* was markedly reduced in the absence of STING (Fig. 2B), with this effect being more pronounced in CLPP-KO/IFNAR-KO MEFs. Ablation of elevated IFN-I signaling was also observed in RNA extracts from tissues of the double mutant crosses, as qRT-PCR analysis of heart (Fig. 2C) and liver (Fig. S2B) showed diminished ISG expression in double KO mice compared to CLPP-KO alone. A similar effect was observed in antiviral proteins such as RIG-I, STAT1, ZBP1, and IFIT3 in heart extracts (Fig. 2D), with marked decreases in all ISGs in CLPP-KO/STING$^{gt/gt}$ and CLPP-KO/IFNAR-KO mice compared to CLPP-KO alone. Although ablation of STING and IFNAR was sufficient to blunt the steady state ISGs signature in CLPP-KO cells and tissues, loss of STING or IFNAR signaling was not sufficient to rescue the growth deficits and small testes size of CLPP-KO mice (Fig. S2C) Moreover, STING depletion did not significantly impact body composition changes (i.e. fat/lean ratio via EchoMRI) resulting from loss of CLPP (Fig. S2D).

## CLPP-KO cells are more resistant to viral infection owing to elevated activation of the STING pathway.

To next assess if basal cGAS-STING-IFN-I signaling and increased steady state expression ISGs in CLPP-KO cells is functionally relevant, we infected MEFs with recombinant Vesicular Stomatitis Virus (VSV) expressing the viral protein VSV-G fused to GFP (VSV-G/GFP) (19). After infection at a MOI of 0.1 for 24h, microscopic analysis showed a striking absence of GFP fluorescence in CLPP-KO cells compared to WT controls (Fig. 3A). Quantification of GFP (Fig. S3A) indicated that only 1.3% of CLPP-KO cells were positive for GFP compared to 25% of WT cells. STING$^{gt/gt}$ cells were more susceptible to VSV

infection consistent with prior results (27, 28), with more than 60% of cells staining GFP positive. Similarly, 68% of CLPP-KO/STING$^{gt/gt}$ cells were GFP positive, indicating that viral resistance of CLPP-KO cells was completely lost in CLPP-KO/STING$^{gt/gt}$ MEFs. Relative levels of viral RNA transcripts for *VSV-G* and *VSV-M* were reduced greater than 95% in CLPP-KO cells compared to WTs (Fig. 3B). In contrast, viral transcript levels were equally high in VSV-infected STING$^{gt/gt}$ and CLPP-KO/STING$^{gt/gt}$ cells. Similar results were found at earlier VSV infection timepoints (i.e. 16 hpi, Fig. S3B), corroborating microscopic results demonstrating that antiviral phenotypes of CLPP-KO cells are mediated by STING signaling.

At 24hpi, there was a striking reduction of viral plaques in CLPP-KO MEFs (2-log reduction) compared to WTs. This contrasted strongly with CLPP-KO/STING$^{gt/gt}$ cells, which exhibited only a small, 1.7-fold reduction compared to STING$^{gt/gt}$ littermate MEFs. The viral protection observed in CLPP-KO cells is likely due to both elevated baseline and induced ISGs, as levels of antiviral genes *Usp18* and *Cmpk2* were further enhanced in CLPP-KO over WT controls after VSV infection (Fig. S3C). Although the VSV-mediated upregulation of ISGs in CLPP-KO cells was greatly blunted by loss of STING, the fold induction of ISGs in double mutant CLPP-KO/STING$^{gt/gt}$ MEFs over infected STING$^{gt/gt}$ MEFs was similar to CLPP-KO over WT cells. RNA viruses such as VSV predominantly engage the RIG-I-MAVS pathway, and although some reports have noted crosstalk between the MAVS and STING pathways, MAVS signaling remains largely functional in the absence of cGAS and STING (29). Thus, the baseline antiviral priming in CLPP-KO cells driven by persistent STING-IFN-I signaling, and not the potentiated induction of ISGs during infection, is likely the most important factor governing the resistance of CLPP-KO cells to VSV.

To determine if the viral resistance extended to DNA viruses, we infected MEF lines with HSV-1, a dsDNA virus that employs several diverse mechanisms to evade innate antiviral responses. After infection at a MOI 0.001 and incubation for 72 hours, HSV-1 viral RNAs *UL30* and *Icp27* were reduced greater than 95% in CLPP-KO MEFs compared to WT controls (Fig. 3D), mirroring findings seen with VSV infections. The dramatic reduction in HSV-1 RNA expression in CLPP-KO cells was lost in double KO cells, and in fact we observed that CLPP-KO/STING$^{gt/gt}$ MEFs exhibited five times more viral RNA transcripts than STING$^{gt/gt}$ littermates (Fig. 3D). This marked increase in viral RNAs in the double KO cells was not observed in VSV infections, where there was only a minor increase in viral transcripts in CLPP-KO/STING$^{gt/gt}$ MEFs over infected STING$^{gt/gt}$ MEFs (Fig. 3C). A similar trend was observed in quantification of viral particles by plaque assays, as we observed resistance of CLPP-KO cells to HSV-1 (1.5 log reduction in plaques) compared to WT cells (Fig. 3E). However, CLPP-KO/STING$^{gt/gt}$ cells were more susceptible to HSV-1 infection (0.5 log increase in plaques) compared to STING$^{gt/gt}$, consistent with viral RNA expression data.

We next assessed whether the strong antiviral response was maintained at a higher and more lytic MOI, where HSV-1 virulence and IFN-I-repressive mechanisms are more potent. At a MOI of 0.01 48hpi, CLPP-KO cells remained more resistant to HSV-1, albeit to a lesser extent compared to infection with a lower MOI (Fig. S3D). CLPP-KO cells showed a 40%

reduction in *UL30* and *Icp27* expression compared to WTs. However, similar to results from MOI 0.001 infections, CLPP-KO/STING$^{gt/gt}$ MEFs exhibited 5 times more viral RNA than STING$^{gt/gt}$ cells (Fig. S3D). Collectively, these results show that potentiated cGAS-STING-dependent IFN-I responses in CLPP deficient cells promote a robust antiviral state that is broadly restrictive to both RNA and DNA viruses.

### CLPP deficiency results in altered mtDNA abundance and nucleoid morphology.

Our prior work has documented that mtDNA stress and cytosolic release is a potent inducer of IFN-I responses via the cGAS-STING DNA sensing axis (21). Since the ISG and antiviral priming phenotypes in CLPP-KO cells and tissues were dependent on cGAS-STING, we hypothesized that mtDNA might be the mitochondrial DAMP triggering this response. Interestingly, we found that MEFs and tissues (10) from CLPP-KO mice exhibit baseline elevations in mtDNA abundance by qPCR-based approaches (Fig. S4A), accompanied by a slight upregulation in Transcription factor A mitochondrial (TFAM) protein levels (Fig. 4D), but no coordinate increase in full-length mtDNA genomes (7). We reasoned that this might indicate the presence of mtDNA instability in CLPP deficient cells. In agreement with this hypothesis, we observed that CLPP-KO MEFs (Fig. 4A) and CLPP-depleted human fibroblasts (Fig. S4B) displayed significant mtDNA nucleoid enlargement and aggregation by confocal microscopy. Indeed, quantification of nucleoids by confocal microscopy revealed markedly more mtDNA stress, as measured by a greater number of enlarged nucleoids (>450nm$^2$ in area), in CLPP-KO MEFs compare to WT cells (Fig. 4B, Fig. S4D). These results are similar to the mtDNA stress phenotype observed in *Tfam*$^{+/-}$ MEFs, which have enlarged mtDNA nucleoids and mitochondrial network hyperfusion that result in the release and cytosolic accumulation of mtDNA, tonic cGAS-STING-IFN-I signaling, and antiviral priming (21).

### mtDNA mediates IFN-I responses in CLPP deficient fibroblasts.

To next demonstrate that mtDNA is the DAMP triggering ISG responses in CLPP-KO MEFs, we treated cells with dideoxycytidine (ddC), a nucleoside reverse transcriptase inhibitor that specifically inhibits mtDNA replication and causes robust mtDNA depletion with little effect on nuclear DNA (30). Notably, ddC treatment was sufficient to clear the enlarged/aggregated nucleoids in CLPP-KO MEFs (Fig. 4A–B), as well as robustly reduce mtDNA levels (Fig. S4C) and nucleoid size (Fig. S4D). Consistent with the notion that mtDNA stress is driving cGAS-STING-IFN-I signaling in CLPP-KO cells, the pronounced ISG signature observed in CLPP-KO MEFs was markedly reduced at the RNA and protein levels after ddC treatment (Fig. 4C–D). In a complementary approach, we transfected MEFs with siRNA against *Polg2* to knockdown the accessory subunit of the mtDNA polymerase pol γ that is required for mtDNA replication (31). Consistent with ddC results, we observed a significant reduction in ISG transcripts in CLPP-KO cells when *Polg2* was knocked down (Fig. 4E).

Recently, it was described that VBIT-4, an inhibitor of voltage-dependent anion channel (VDAC) oligomerization, blocks the formation of mitochondrial pores and prevents the release of mtDNA fragments into the cytosol of *Endog* deficient MEFs (32). We next tested this reagent in our MEF lines, and similar to the results with ddC treatment and *Polg2*

knockdown, VBIT-4 treatment significantly diminished the strong ISG signature of CLPP-KO MEFs at baseline (Fig. 4F). VBIT-4 had no effect on ISG expression induced by recombinant mIFNβ treatment (Fig. S4E), indicating that the abrogation of steady state antiviral responses by VBIT-4 was not due to a general suppression of IFN-I signaling in CLPP-KO cells. Collectively, these results document that mtDNA stress and VDAC-mediated mtDNA release into the cytosol are key triggers of cGAS-STING-IFN-I signaling and antiviral responses in CLPP-KO cells.

Finally, we explored other factors that modulate mtDNA stress and/or signaling to IFN-I in order to rule in or out their involvement in the enhanced ISG signature of CLPP-KO cells. Interestingly, CLPX, the chaperone and ATPase from the protease complex CLPXP, has been associated with maintenance of mtDNA nucleoids in human cells (33). Although CLPX is upregulated in CLPP null cells, we found that siRNA knockdown of CLPX had no effect on nucleoid aggregation (data not shown) or steady state ISG responses in CLPP-KO MEFs (Fig. 5A). We next employed siRNA approaches to target both mitochondrial fusion and fission proteins, since mitochondrial dynamics facilitate proper nucleoid distribution and removal of damaged mtDNA (34, 35). However, we found that transient downregulation of mitofusin 1 (Mfn1) or the fission factor dynamin-related protein 1 (Drp1) did not significantly alter the ISG signature in CLPP-KO cells (Fig. 5B). Lastly, to assess whether the ISG signature in CLPP null cells is due to altered translation and/or accumulation of misfolded mtDNA-encoded proteins, we treated cells with chloramphenicol (CAM), a mitochondrial translation inhibitor, and measured ISG levels by western blotting after kinetic exposure. Exposures of low (50μM) to high (200μM) concentrations and durations of 24h to 48h revealed that while CAM treatment robustly inhibited mitochondrial translation (as seen by significant reductions in mt-COI protein levels), it had no effect on the elevated steady state ISG signature of CLPP-KO cells (Fig. 5C).

## DISCUSSION

Caseinolytic peptidase XP (ClpXP) is an evolutionarily conserved, heteromeric, mitochondrial matrix localized serine protease complex, and despite extensive studies on prokaryotic ClpXP, the diverse functions of CLPXP in mitochondria remain less well defined (36). CLPP null phenotypes in mice mirror human Perrault syndrome (PS), displaying growth retardation, deafness, and premature sterility (10). Interestingly, CLPP-KO mice show immune alterations, with elevated expression of ISGs observed in peripheral tissues and fibroblasts (10, 18). However, the mitochondrial molecular mechanisms and innate immune signaling pathways underlying activation of antiviral signatures in CLPP-KO mice have not been defined, and the biological significance of immune alterations in CLPP deficient cells and tissues has remained unclear.

Our results indicate that loss of CLPP in human and murine engages IFN-I responses via the cGAS-STING axis. Moreover, we have found that the primed IFN-I state of CLPP-KO cells is functionally relevant, conferring robust resistance to both RNA and DNA viruses (Fig. 5D). Similar viral resistance phenotypes have been reported in other cell lines with chronically activated IFN-I responses. Studies on cells lacking the exonuclease TREX1 or endoribonuclease RNaseH2, as well on *Tfam*$^{+/-}$ MEFs, have revealed that baseline priming

of IFN-I responses is sufficient to protect these cells from viral infection (21, 37–39). Similar to TREX1-, RNaseH2-, and TFAM-deficient cells, we have found that the viral resistance of CLPP-KO cells is mediated by baseline activation of the cGAS-STING pathway, since protection against VSV and HSV-1 infection is lost in CLPP-KO/STING$^{gt/gt}$ cells. The interesting finding that CLPP-KO/STING$^{gt/gt}$ MEFs are more susceptible to HSV-1 infection may be due to the fact that HSV-1 is a robust modulator of host mitochondrial function and metabolism (40, 41). We hypothesize that the complete lack of cytosolic DNA sensing and antiviral IFN-I, combined with altered mitochondrial homeostasis in CLPP-KO/STING$^{gt/gt}$ cells, likely synergize to increase HSV-1 virulence mechanisms and increase viral replication. Notably, HSV-1 can directly target host mtDNA through the virally-encoded deoxyribonuclease UL12.5, resulting in nucleoid stress/enlargement followed by rapid mtDNA depletion (21, 42, 43). Thus, increased interference with mtDNA homeostasis by UL12.5 or other encoded factors may potentially explain the elevated susceptibility of double KO cells to HSV-1.

We have also uncovered the novel finding that loss of CLPP alters mtDNA homeostasis. While more than 50 nucleoid-associated proteins have been shown to participate in mtDNA maintenance and gene expression, CLPP has not yet been implicated in either process (44). Our findings document that CLPP is necessary for maintaining mtDNA nucleoid organization and distribution, as CLPP null cells exhibit markedly disrupted nucleoid architecture and TFAM aggregation compared to WT cells. Of note, a recent clinical study revealed decreased *CLPP* mRNA levels and increased mtDNA abundance and in patient fibroblasts harboring disease-associated *CLPP* mutations (45). Combined with our results in CLPP deficient cells, these findings collectively suggest a conserved role for CLPP in regulation of mtDNA maintenance and a potential role for mtDNA stress in the pathogenesis of PS. However, our CLPP knockdown and knockout fibroblasts do not exactly phenocopy patient cells harboring *CLPP* missense mutations associated with PS. These disease mutations are noted to alter key amino acids in a cluster near the docking site for CLPX interaction or in the active site of the peptidase (46). Future work to re-introduce synonymous pathogenic mutant CLPP proteins into CLPP-KO mice or to generate germline mutations in *Clpp* via CRISPR/Cas9 will help to determine how these disease relevant mutations contribute to mtDNA instability, IFN-I responses, and PS disease pathogenesis.

We found that treatment with ddC or siRNA against the pol γ accessory subunit, Polg2, to deplete mtDNA and aberrant nucleoids markedly reduced ISG responses of CLPP-KO cells. Moreover, blocking direct mtDNA release via VDAC was sufficient to ablate steady state expression of ISGs in CLPP-KO MEFs. These results strongly indicate that mtDNA instability and escape into the cytosol are key upstream triggers of cGAS-STING-IFN-I signaling in cells lacking CLPP. It is also noteworthy that mono-allelic loss of another matrix protease and mtDNA maintenance factor, LONP1, leads to steady state induction of ISGs in MEFs (18). This indicates that perturbations in mitochondrial matrix protease levels, which disrupt mtDNA homeostasis and stability, generally engage IFN-I signaling, thus linking mammalian UPR$^{mt}$ factors to antiviral innate immunity (5, 47, 48). In addition, another study identified ERAL1, a putative 12S rRNA chaperone, as a CLPXP substrate, implicating CLPP in mitoribosomal assembly and mitochondrial translation (7). Although mitoribosomal maturation/assembly was not analyzed carefully in this study, treatment with

CAM to inhibit mitochondrial translation did not bring down steady state IFN-I responses or lessen the aberrant nucleoid morphology in CLPP-KO cells (data not shown). Future studies aimed at uncovering the molecular mechanisms by which CLPP integrates mitoribosomal assembly, proteostasis, mitochondrial nucleoid organization, and mtDNA release should yield new insight into crosstalk between the mammalian $UPR^{mt}$ and the innate immune system.

CLPP-KO mice exhibit reduced adiposity, increased whole-body energy expenditure, and protection from diet-induced obesity, indicating a role of CLPP in metabolic rewiring (12). Although deletion of STING or IFNAR ablated the ISG signature in CLPP-KO tissues, loss of either protein in vivo was not sufficient to rescue the small body size of CLPP-KO mice. Moreover, body composition analysis revealed that deletion of STING did not rescue the decreased fat/increased lean mass observed in CLPP-KO mice. Although our study does not directly address the role of STING-IFN-I signaling in infertility or deafness in CLPP-KO mice, we did find that the small testis size observed in CLPP-KO mice was not rescued by ablation of STING or IFNAR. However, several studies have linked IFN-I to sterility in both transgenic mouse models and human patients receiving exogenous IFN-α therapy (49–51). Moreover, sudden hearing loss has been reported as an adverse effect of IFN-α immunotherapy in patients with hepatitis C virus or cancer (52, 53). Therefore, it will be interesting to more carefully explore whether ablation of STING or IFNAR in CLPP-KO mice impacts the development or progression of sterility and/or deafness, which may have implications for understanding the role of STING-IFN-I signaling in the diverse pathology of human PS.

In conclusion, our results place the cGAS-STING-IFN-I innate immune pathway downstream of CLPP and illuminate new links between mitochondrial proteostasis, mtDNA genome maintenance, and antiviral immunity. Imbalances in mitochondrial protease function, mtDNA damage, and innate immunity are each associated with various pathological conditions, such as neurodegenerative disorders, infertility, metabolic syndromes, and cancer (36, 54). This work sheds new light on the biology of mammalian CLPP, further advances our understanding of mitochondrial-innate immune crosstalk, and may have implications for understanding PS pathogenesis and other diseases involving CLPP dysregulation.

## Supplementary Material

Refer to Web version on PubMed Central for supplementary material.

## ACKNOWLEDGEMENTS

We would like to thank our colleagues in the West Lab for feedback on the manuscript, as well as Dr. Malea Murphy in the Integrated Microscopy and Imaging Laboratory at the Texas A&M College of Medicine for assistance with confocal imaging.

This research was supported by awards W81XWH-17-1-0052 and W81XWH-20-1-0150 to A.P.W. from the Office of the Assistant Secretary of Defense for Health Affairs through the Peer Reviewed Medical Research Programs. Additional support was provided by NIH grant R01HL148153 to A.P.W. Opinions, interpretations, conclusions, and recommendations are those of the author and are not necessarily endorsed by the NIH or Department of Defense.

## REFERENCES


1. Quirós PM, Langer T, and López-Otín C. 2015. New roles for mitochondrial proteases in health, ageing and disease. Nat. Rev. Mol. Cell Biol 16: 345–359. [PubMed: 25970558]
2. Baker TA, and Sauer RT. 2012. ClpXP, an ATP-powered unfolding and protein-degradation machine. Biochim. Biophys. Acta 1823: 15–28. [PubMed: 21736903]
3. Bhandari V, Wong KS, Zhou JL, Mabanglo MF, Batey RA, and Houry WA. 2018. The Role of ClpP Protease in Bacterial Pathogenesis and Human Diseases. ACS Chem. Biol 13: 1413–1425. [PubMed: 29775273]
4. Haynes CM, Petrova K, Benedetti C, Yang Y, and Ron D. 2007. ClpP mediates activation of a mitochondrial unfolded protein response in C. elegans. Dev. Cell 13: 467–480. [PubMed: 17925224]
5. Pellegrino MW, Nargund AM, Kirienko NV, Gillis R, Fiorese CJ, and Haynes CM. 2014. Mitochondrial UPR-regulated innate immunity provides resistance to pathogen infection. Nature 516: 414–417. [PubMed: 25274306]
6. Deepa SS, Bhaskaran S, Ranjit R, Qaisar R, Nair BC, Liu Y, Walsh ME, Fok WC, and Van Remmen H. 2016. Down-regulation of the mitochondrial matrix peptidase ClpP in muscle cells causes mitochondrial dysfunction and decreases cell proliferation. Free Radic. Biol. Med 91: 281–292. [PubMed: 26721594]
7. Szczepanowska K, Maiti P, Kukat A, Hofsetz E, Nolte H, Senft K, Becker C, Ruzzenente B, Hornig-Do H-T, Wibom R, Wiesner RJ, Krüger M, and Trifunovic A. 2016. CLPP coordinates mitoribosomal assembly through the regulation of ERAL1 levels. EMBO J 35: 2566–2583. [PubMed: 27797820]
8. Ishizawa J, Zarabi SF, Davis RE, Halgas O, Nii T, Jitkova Y, Zhao R, St-Germain J, Heese LE, Egan G, Ruvolo VR, Barghout SH, Nishida Y, Hurren R, Ma W, Gronda M, Link T, Wong K, Mabanglo M, Kojima K, Borthakur G, MacLean N, Ma MCJ, Leber AB, Minden MD, Houry W, Kantarjian H, Stogniew M, Raught B, Pai EF, Schimmer AD, and Andreeff M. 2019. Mitochondrial ClpP-Mediated Proteolysis Induces Selective Cancer Cell Lethality. Cancer Cell 35: 721–737.e9. [PubMed: 31056398]
9. Graves PR, Aponte-Collazo LJ, Fennell EMJ, Graves AC, Hale AE, Dicheva N, Herring LE, Gilbert TSK, East MP, McDonald IM, Lockett MR, Ashamalla H, Moorman NJ, Karanewsky DS, Iwanowicz EJ, Holmuhamedov E, and Graves LM. 2019. Mitochondrial Protease ClpP is a Target for the Anticancer Compounds ONC201 and Related Analogues. ACS Chem. Biol 14: 1020–1029. [PubMed: 31021596]
10. Gispert S, Parganlija D, Klinkenberg M, Dröse S, Wittig I, Mittelbronn M, Grzmil P, Koob S, Hamann A, Walter M, Büchel F, Adler T, Hrabé de Angelis M, Busch DH, Zell A, Reichert AS, Brandt U, Osiewacz HD, Jendrach M, and Auburger G. 2013. Loss of mitochondrial peptidase Clpp leads to infertility, hearing loss plus growth retardation via accumulation of CLPX, mtDNA and inflammatory factors. Hum. Mol. Genet 22: 4871–4887. [PubMed: 23851121]
11. Jenkinson EM, Rehman AU, Walsh T, Clayton-Smith J, Lee K, Morell RJ, Drummond MC, Khan SN, Naeem MA, Rauf B, Billington N, Schultz JM, Urquhart JE, Lee MK, Berry A, Hanley NA, Mehta S, Cilliers D, Clayton PE, Kingston H, Smith MJ, Warner TT, University of Washington Center for Mendelian Genomics, Black GC, Trump D, Davis JRE, Ahmad W, Leal SM, Riazuddin S, King M-C, Friedman TB, and Newman WG. 2013. Perrault syndrome is caused by recessive mutations in CLPP, encoding a mitochondrial ATP-dependent chambered protease. Am. J. Hum. Genet 92: 605–613. [PubMed: 23541340]
12. Bhaskaran S, Pharaoh G, Ranjit R, Murphy A, Matsuzaki S, Nair BC, Forbes B, Gispert S, Auburger G, Humphries KM, Kinter M, Griffin TM, and Deepa SS. 2018. Loss of mitochondrial protease ClpP protects mice from diet-induced obesity and insulin resistance. EMBO Rep 19.
13. Wang T, Babayev E, Jiang Z, Li G, Zhang M, Esencan E, Horvath T, and Seli E. 2018. Mitochondrial unfolded protein response gene Clpp is required to maintain ovarian follicular reserve during aging, for oocyte competence, and development of pre-implantation embryos. Aging Cell 17: e12784. [PubMed: 29851234]

14. Becker C, Kukat A, Szczepanowska K, Hermans S, Senft K, Brandscheid CP, Maiti P, and Trifunovic A. 2018. CLPP deficiency protects against metabolic syndrome but hinders adaptive thermogenesis. EMBO Rep 19: e45126. [PubMed: 29588285]
15. West AP, and Shadel GS. 2017. Mitochondrial DNA in innate immune responses and inflammatory pathology. Nat. Rev. Immunol 17: 363–375. [PubMed: 28393922]
16. Nakahira K, Hisata S, and Choi AMK. 2015. The Roles of Mitochondrial Damage-Associated Molecular Patterns in Diseases. Antioxid. Redox Signal 23: 1329–1350. [PubMed: 26067258]
17. Youle RJ 2019. Mitochondria—Striking a balance between host and endosymbiont. Science 365.
18. Key J, Maletzko A, Kohli A, Gispert S, Torres-Odio S, Wittig I, Heidler J, Bárcena C, López-Otín C, Lei Y, West AP, Münch C, and Auburger G. 2020. Loss of mitochondrial ClpP, Lonp1, and Tfam triggers transcriptional induction of Rnf213, a susceptibility factor for moyamoya disease. neurogenetics 21: 187–203. [PubMed: 32342250]
19. Dalton KP, and Rose JK. 2001. Vesicular stomatitis virus glycoprotein containing the entire green fluorescent protein on its cytoplasmic domain is incorporated efficiently into virus particles. Virology 279: 414–421. [PubMed: 11162797]
20. Desai P, and Person S. 1998. Incorporation of the green fluorescent protein into the herpes simplex virus type 1 capsid. J. Virol 72: 7563–7568. [PubMed: 9696854]
21. West AP, Khoury-Hanold W, Staron M, Tal MC, Pineda CM, Lang SM, Bestwick M, Duguay BA, Raimundo N, MacDuff DA, Kaech SM, Smiley JR, Means RE, Iwasaki A, and Shadel GS. 2015. Mitochondrial DNA stress primes the antiviral innate immune response. Nature 520: 553–557. [PubMed: 25642965]
22. Key J, Kohli A, Bárcena C, López-Otín C, Heidler J, Wittig I, and Auburger G. 2019. Global Proteome of LonP1+/− Mouse Embryonal Fibroblasts Reveals Impact on Respiratory Chain, but No Interdependence between Eral1 and Mitoribosomes. Int. J. Mol. Sci 20.
23. Cox J, and Mann M. 2008. MaxQuant enables high peptide identification rates, individualized p.p.b.-range mass accuracies and proteome-wide protein quantification. Nat. Biotechnol 26: 1367–1372. [PubMed: 19029910]
24. Volkman HE, Cambier S, Gray EE, and Stetson DB. 2019. Tight nuclear tethering of cGAS is essential for preventing autoreactivity. eLife 8.
25. Rongvaux A, Jackson R, Harman CCD, Li T, West AP, de Zoete MR, Wu Y, Yordy B, Lakhani SA, Kuan C-Y, Taniguchi T, Shadel GS, Chen ZJ, Iwasaki A, and Flavell RA. 2014. Apoptotic caspases prevent the induction of type I interferons by mitochondrial DNA. Cell 159: 1563–1577. [PubMed: 25525875]
26. Dhir A, Dhir S, Borowski LS, Jimenez L, Teitell M, Rötig A, Crow YJ, Rice GI, Duffy D, Tamby C, Nojima T, Munnich A, Schiff M, de Almeida CR, Rehwinkel J, Dziembowski A, Szczesny RJ, and Proudfoot NJ. 2018. Mitochondrial double-stranded RNA triggers antiviral signalling in humans. Nature 560: 238–242. [PubMed: 30046113]
27. Franz KM, Neidermyer WJ, Tan Y-J, Whelan SPJ, and Kagan JC. 2018. STING-dependent translation inhibition restricts RNA virus replication. Proc. Natl. Acad. Sci 115: E2058–E2067. [PubMed: 29440426]
28. Ahn J, and Barber GN. 2019. STING signaling and host defense against microbial infection. Exp. Mol. Med 51: 1–10.
29. Zevini A, Olagnier D, and Hiscott J. 2017. Cross-Talk between the Cytoplasmic RIG-I and STING Sensing Pathways. Trends Immunol 38: 194–205. [PubMed: 28073693]
30. Kasashima K, Sumitani M, and Endo H. 2011. Human mitochondrial transcription factor A is required for the segregation of mitochondrial DNA in cultured cells. Exp. Cell Res 317: 210–220. [PubMed: 20955698]
31. Young MJ, and Copeland WC. 2016. Human mitochondrial DNA replication machinery and disease. Curr. Opin. Genet. Dev 38: 52–62. [PubMed: 27065468]
32. Kim J, Gupta R, Blanco LP, Yang S, Shteinfer-Kuzmine A, Wang K, Zhu J, Yoon HE, Wang X, Kerkhofs M, Kang H, Brown AL, Park S-J, Xu X, van Rilland EZ, Kim MK, Cohen JI, Kaplan MJ, Shoshan-Barmatz V, and Chung JH. 2019. VDAC oligomers form mitochondrial pores to release mtDNA fragments and promote lupus-like disease. Science 366: 1531–1536. [PubMed: 31857488]

33. Kasashima K, Sumitani M, and Endo H. 2012. Maintenance of mitochondrial genome distribution by mitochondrial AAA+ protein ClpX. Exp. Cell Res 318: 2335–2343. [PubMed: 22841477]
34. Ban-Ishihara R, Ishihara T, Sasaki N, Mihara K, and Ishihara N. 2013. Dynamics of nucleoid structure regulated by mitochondrial fission contributes to cristae reformation and release of cytochrome c. Proc. Natl. Acad. Sci. U. S. A 110: 11863–11868. [PubMed: 23821750]
35. Malena A, Loro E, Di Re M, Holt IJ, and Vergani L. 2009. Inhibition of mitochondrial fission favours mutant over wild-type mitochondrial DNA. Hum. Mol. Genet 18: 3407–3416. [PubMed: 19561330]
36. Levytskyy RM, Germany EM, and Khalimonchuk O. 2016. Mitochondrial Quality Control Proteases in Neuronal Welfare. J. Neuroimmune Pharmacol. Off. J. Soc. NeuroImmune Pharmacol 11: 629–644.
37. Hasan M, Gonugunta VK, Dobbs N, Ali A, Palchik G, Calvaruso MA, DeBerardinis RJ, and Yan N. 2017. Chronic innate immune activation of TBK1 suppresses mTORC1 activity and dysregulates cellular metabolism. Proc. Natl. Acad. Sci 114: 746–751. [PubMed: 28069950]
38. Schoggins JW, Wilson SJ, Panis M, Murphy MY, Jones CT, Bieniasz P, and Rice CM. 2011. A diverse range of gene products are effectors of the type I interferon antiviral response. Nature 472: 481–485. [PubMed: 21478870]
39. Pokatayev V, Hasin N, Chon H, Cerritelli SM, Sakhuja K, Ward JM, Morris HD, Yan N, and Crouch RJ. 2016. RNase H2 catalytic core Aicardi-Goutières syndrome–related mutant invokes cGAS–STING innate immune-sensing pathway in mice. J. Exp. Med 213: 329–336. [PubMed: 26880576]
40. Duarte LF, Farías MA, Álvarez DM, Bueno SM, Riedel CA, and González PA. 2019. Herpes Simplex Virus Type 1 Infection of the Central Nervous System: Insights Into Proposed Interrelationships With Neurodegenerative Disorders. Front. Cell. Neurosci 13.
41. Reshi L, Wang H-V, and Hong J-R. 2018. Modulation of Mitochondria During Viral Infections. Mitochondrial Dis Taskin E, Guven C and Sevgiler Y, IntechOpen. https://www.intechopen.com/books/mitochondrial-diseases/modulation-of-mitochondria-during-viral-infections
42. Saffran HA, Pare JM, Corcoran JA, Weller SK, and Smiley JR. 2007. Herpes simplex virus eliminates host mitochondrial DNA. EMBO Rep 8: 188–193. [PubMed: 17186027]
43. Corcoran JA, Saffran HA, Duguay BA, and Smiley JR. 2009. Herpes simplex virus UL12.5 targets mitochondria through a mitochondrial localization sequence proximal to the N terminus. J. Virol 83: 2601–2610. [PubMed: 19129438]
44. Lee SR, and Han J. 2017. Mitochondrial Nucleoid: Shield and Switch of the Mitochondrial Genome. Oxid. Med. Cell. Longev ID 8060949.
45. Theunissen TEJ, Szklarczyk R, Gerards M, Hellebrekers DMEI, Mulder-Den Hartog ENM, Vanoevelen J, Kamps R, de Koning B, Rutledge SL, Schmitt-Mechelke T, van Berkel CGM, van der Knaap MS, de Coo IFM, and Smeets HJM. 2016. Specific MRI Abnormalities Reveal Severe Perrault Syndrome due to CLPP Defects. Front. Neurol 7:203. [PubMed: 27899912]
46. Brodie EJ, Zhan H, Saiyed T, Truscott KN, and Dougan DA. 2018. Perrault syndrome type 3 caused by diverse molecular defects in CLPP. Sci. Rep 8: 12862. [PubMed: 30150665]
47. Wang S, Gao K, and Liu Y. 2018. UPRmt coordinates immunity to maintain mitochondrial homeostasis and animal fitness. Mitochondrion 41: 9–13. [PubMed: 29180055]
48. Melber A, and Haynes CM. 2018. UPRmt regulation and output: a stress response mediated by mitochondrial-nuclear communication. Cell Res 28: 281–295. [PubMed: 29424373]
49. Ulusoy E, Çayan S, Yilmaz N, Aktaş S, Acar D, and Doruk E. 2004. Interferon α−2b may impair testicular histology including spermatogenesis in a rat model. Arch. Androl 50: 379–385. [PubMed: 15551753]
50. Hekman AC, Trapman J, Mulder AH, van Gaalen JL, and Zwarthoff EC. 1988. Interferon expression in the testes of transgenic mice leads to sterility. J. Biol. Chem 263: 12151–12155. [PubMed: 3403564]
51. Iwakura Y, Asano M, Nishimune Y, and Kawade Y. 1988. Male sterility of transgenic mice carrying exogenous mouse interferon-beta gene under the control of the metallothionein enhancer-promoter. EMBO J 7: 3757–3762. [PubMed: 3208748]

52. Asal S, Sobhy O, Ismail O, and Bedewy E. 2014. Study of the effect of combined interferon and ribavirin therapy on the hearing profile of hepatitis C virus patients. Egypt J Otolaryngol 31, 4: 237–243.

53. Formann E, Stauber R, Denk D-M, Jessner W, Zollner G, Munda-Steindl P, Gangl A, and Ferenci P. 2004. Sudden Hearing Loss in Patients with Chronic Hepatitis C Treated with Pegylated Interferon/Ribavirin. Am. J. Gastroenterol 99: 873–877. [PubMed: 15128353]

54. Barcena C, Mayoral P, Quiros P, and Lopez-Otin C. 2017. Physiological and Pathological Functions of Mitochondrial Proteases. In: Chakraborti S, Dhalla N (eds) Proteases in Physiology and Pathology Springer, Singapore

**KEY POINTS**

- IFN-I signaling in CLPP-deficient cells and tissues depends on cGAS and STING.
- CLPP-deficient cells are resistant to DNA and RNA viruses due to elevated ISGs.
- CLPP-deficient cells exhibit mitochondrial DNA stress and release into the cytosol.

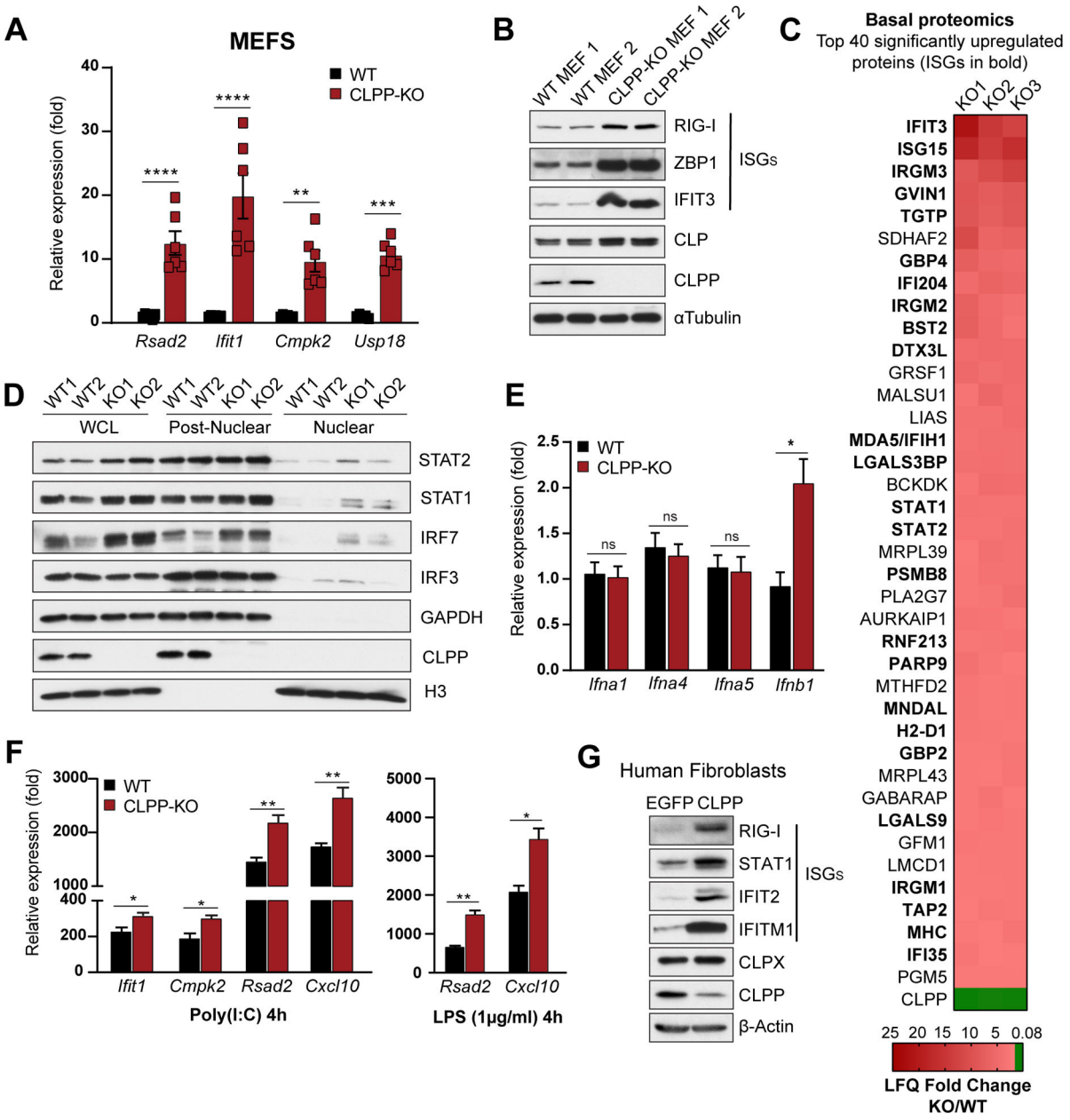


**Figure 1. CLPP deficiency leads to steady state interferon stimulated gene (ISG) expression in mouse and human cells.**

**(A, B)** Quantitative real-time PCR (**A**) and western blots (**B**) of baseline ISGs of littermate WT and CLPP-KO mouse embryonic fibroblasts (MEFs) lines (n=6 MEF lines per genotype in A and 2 in B). **(C)** Heat map from the top 40 significantly ($p<0.05$) upregulated proteins from baseline proteomic data of littermates WT and CLPP-KO MEFs. Data represented as Label-free quantification (LFQ) fold change of each CLPP-KO MEFs over average WT (n=3 MEF biological replicates). (**D**) Western blotting of baseline transcription factors after subcellular fractionation of WT and CLPP-KO MEFs (n=2 MEF lines). (**E**) Quantitative real-time PCR of type I interferon gene expression in littermate WT and CLPP-KO MEFs (n=2 MEFs lines pooled). (**F**) Quantitative real-time PCR of ISGs in WT and CLPP-KO

MEFs, 4h after transfection with poly(I:C) or LPS challenge. (n=3 biological replicates pooled). (**G**) Human foreskin fibroblasts were transduced with the shRNA against CLPP and EGFP (as control) and selected with puromycin (2μg/ml). After selection, cells were plated in 12-well dishes and harvested for western blots of baseline ISGs. Error bars represent mean ± s.e.m. and all figures are representative of three independent experiments. *p<0.05, **p<0.01, ***p<0.001, ****p<0.0001. In A, two-way ANOVA Tukey's *post-hoc*, and in (E-F) Student's t-test were used to determine significance.

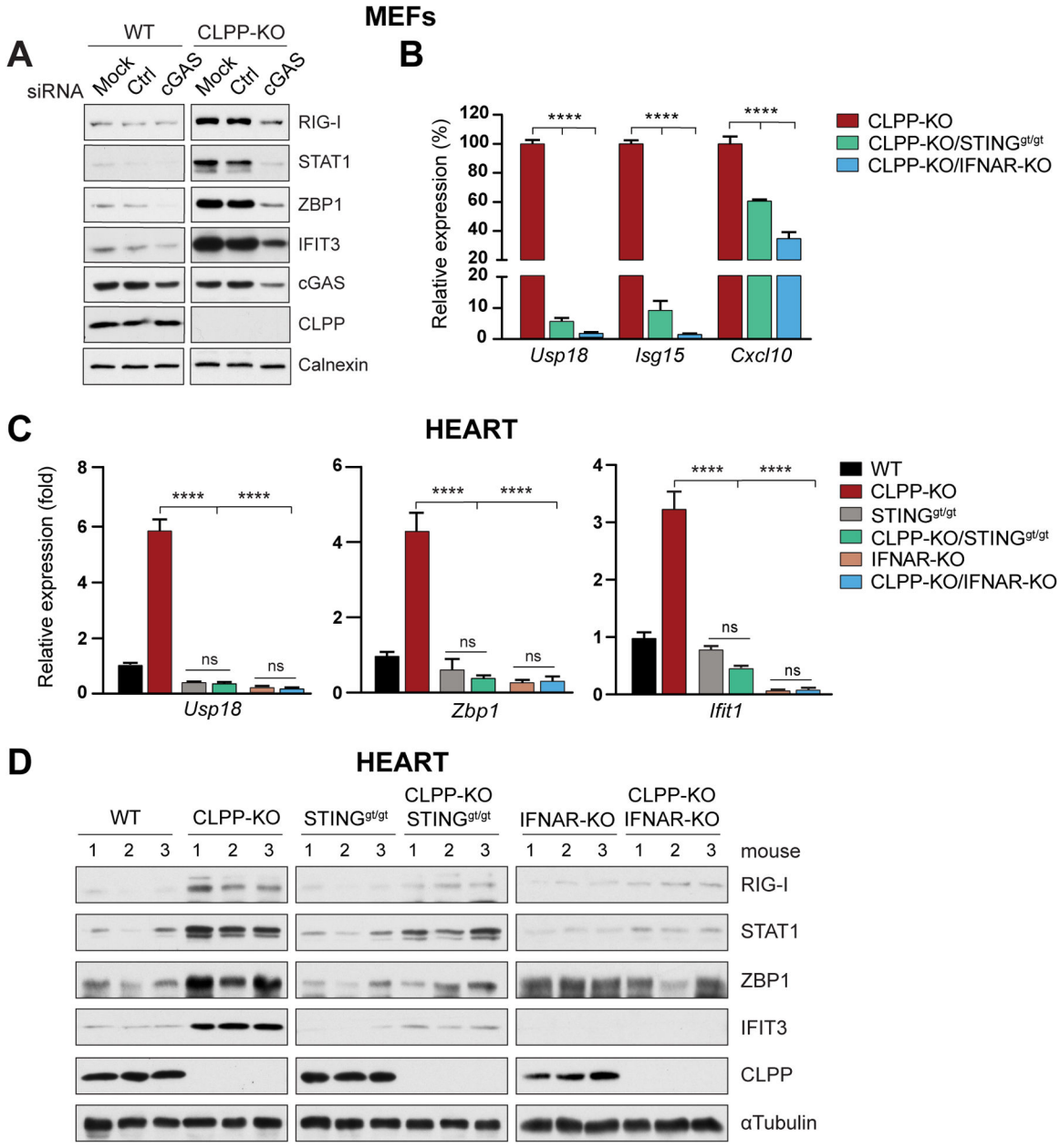


**Figure 2. STING and IFNAR mediate the steady state ISG and antiviral signature in CLPP deficient cells and tissues.**

(**A**) Representative western blots of ISGs in WT and CLPP-KO MEFs transfected with siRNA Control (Ctrl) and sicGAS for 72hrs. Experiment was repeated 3 times with 2 MEF lines. (**B**) Quantitative real-time PCR of baseline ISGs in WT, CLPP-KO, and CLPP-KO/STING$^{gt/gt}$ or CLPP-KO/IFNAR-KO double mutant MEFs. Real-time PCR data was represented as relative expression percentage (%) with CLPP-KO set to 100%. (n=3 biological replicates). (**C, D**) Quantitative real-time PCR (C) and western blots (D) of baseline ISGs from heart tissue from three 12-month old male mice per genotype. Error bars represent as mean ± s.e.m. of triplicates and all figures are representative of three

independent experiments. ***p<0.001, ****p<0.0001, ns, non-significant. One-way ANOVA, Tukey's *post-hoc* was used to determine significance.

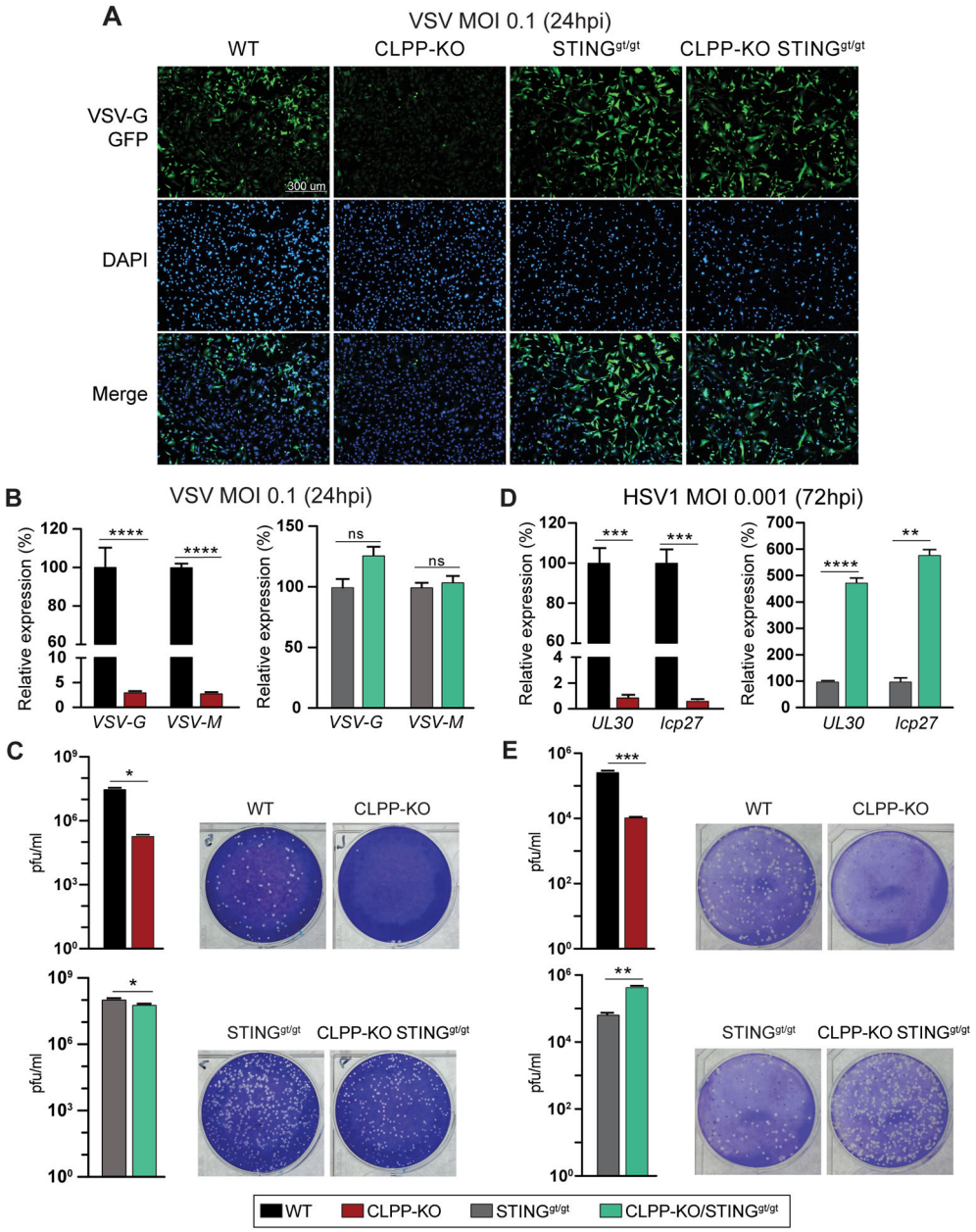


**Figure 3. CLPP-KO fibroblasts are more resistant to viral infection owing to elevated activation of the STING pathway.**

(**A–C**) Analysis of viral load and viral plaques in MEFs after 24hrs of VSV infection at multiplicity of infection (MOI) of 0.1. (**A**) Representative microscopy images of viral GFP expression in MEFs infected with VSV. DAPI was used for nuclear staining. (**B**) Quantitative real-time PCR of viral RNA transcripts, *VSV-G* and *VSV-M*, after VSV infection (n=3 biological replicates per genotype per condition). (**C**) Quantification of plaque assays from VSV infected MEFs. Plaque figure is representative of $10^{-5}$ supernatant dilution and graphed as pfu/ml from triplicate technical replicates. (**D**) Quantitative real-time PCR of viral RNA in MEFs infected with HSV-1 at 72hrs post infection (hpi) and MOI of 0.001 (n=3 biological replicates). (**E**) Quantification of plaque assay from HSV-1 infected

MEFs. Plaque figure is representative of $10^{-2}$ supernatant dilution and graphed as pfu/ml from triplicate technical replicates. In (B, D), real-time PCR data was represented as relative expression percentage (%) comparing CLPP-KO vs WT and CLPP-KO/STING$^{gt/gt}$ vs STING$^{gt/gt}$ MEFs. In (B-E), error bars represent mean ± s.e.m. of triplicates and all experiments are representative of 3–4 independent experiments. **p<0.01, ***p<0.001, ****p<0.0001, ns non-significant (Student's t-test).

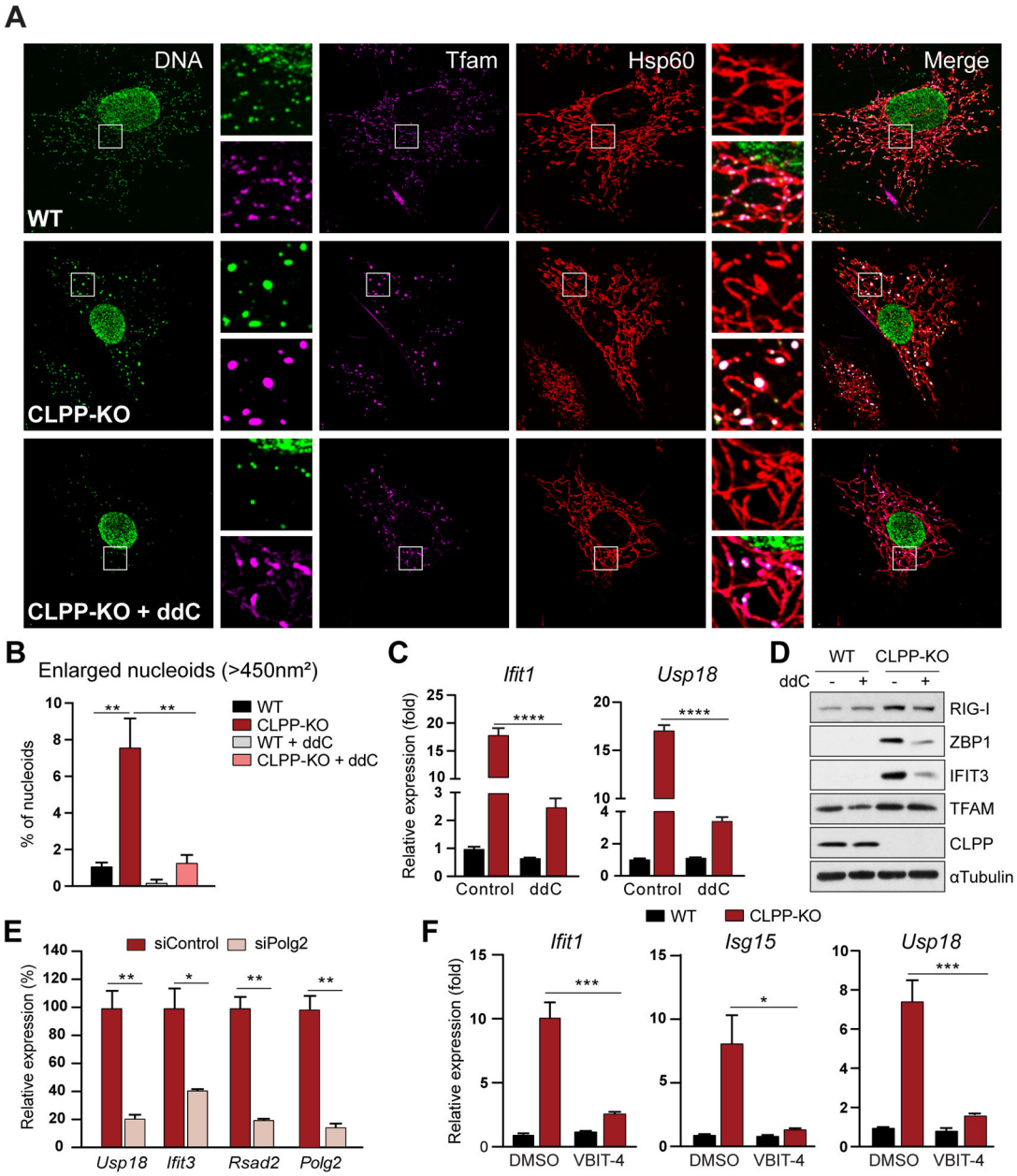


**Figure 4. Altered mtDNA homeostasis mediates IFN-I responses in CLPP-KO fibroblasts.**

(**A–D**) WT and CLPP-KO MEFs were cultured in the presence of regular media (Control) or media containing ddC (150μM). Cells were harvested after 4 days for (**A**) confocal microscopy with anti-DNA (DNA), anti-Tfam (mtDNA nucleoid marker) and anti-HSP60 (mitochondrial matrix protein). (**B**) Nucleoid quantification represented as percentage (%) of enlarged nucleoids (>450nm$^2$). (**C**) Quantitative real-time PCR analysis of ISG expression (n=3 biological replicates). (**D**) Representative western blots of ISG protein expression. (**E**) Quantitative real-time PCR of ISGs in CLPP-KO MEFs transfected with control or siPolg2 siRNA for 72hrs. (n=3 biological replicates). (**F**) Quantitative real-time PCR of ISGs of WT and CLPP-KO MEFs treated with VBIT-4 (10μM) or Control (DMSO) for 48hrs (n=3 biological replicates). In (**E**), real-time PCR data are presented as relative expression

percentage (%) setting siControl as 100%. Error bars represent mean ± s.e.m. of triplicates, Student's t-test. In (C) and (F), error bars represent mean ± s.e.m. of triplicates, two-way ANOVA Tukey's *post-hoc*. *p<0.05, **p<0.01, ****p<0.0001. All experiments are representative of 3–4 independent experiments.

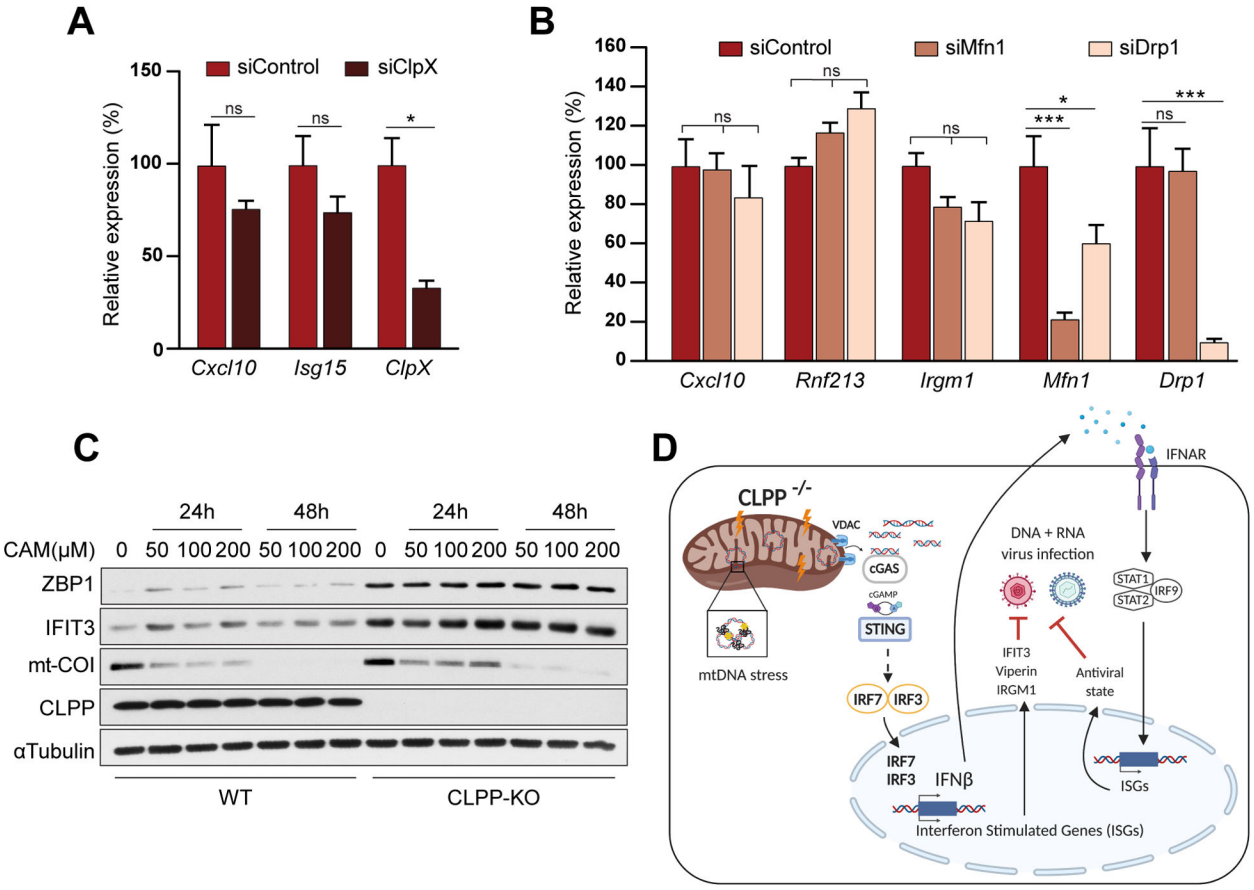


**Figure 5. mtDNA stress-mediated IFN-I responses in CLPP-KO fibroblasts are independent of mitochondrial dynamics and translation.**

(**A, B**) Quantitative real-time PCR of ISGs in CLPP-KO MEFs transfected with siRNA Control (Ctrl) and (**A**) siClpX, or (**B**) siMfn1 and siDrp1 for 72hrs. Real-time PCR data are presented as relative expression percentage (%) considering CLPP-KO siControl as 100% (n=3 biological replicates). (**C**) Representative ISG protein levels of WT and CLPP-KO MEFs treated with chloramphenicol (CAM, 50–200μM) over a 24hr to 48hr time course. (**D**) Graphical abstract showing how absence of CLPP protease leads to mtDNA stress (packaging alterations), cytosolic release of mtDNA through VDAC pores, downstream signaling to the cGAS-STING-IFN-I axis, and broad viral resistance. Error bars represent mean ± s.e.m. of triplicates, and all experiments are representative of 2–3 independent experiments. In (A), Student's t-test was used and in (B), a one-way ANOVA Tukey's *post hoc* was used to determine significance. *p<0.05, **p<0.01, ***p<0.001, ****p<0.0001, ns non-significant.

**Table 1.**

Sequences of primers used for real time PCR.

| | | | |
|---|---|---|---|
| mCmpk2 | AAAGAATCAACCAACTTT<br>GGCCTCCACTCACCTCAGTA | mRsad2 | ATAGTGAGCAATGGCAGGCCT<br>AACCTGCTGATGCAAGCTGT |
| mCxcl10 | CCAAGTGCTGCCGTCATTTTC<br>GGCTCGCAGGGATGATTTCAA | mRp137 | CATCCTTTGGTAAGCGTCGCA<br>TGGCACTCCAGTTATACTTCCT |
| mDrp1 | TCCCAATTCCATTATCCTCGC<br>CATCAGTACCCGCATCCATG | mUsp18 | GAGAGGACCATGAAGAGGA<br>TAAACCAACCAGACCATGAG |
| mIfit1 | CAAGGCAGGTTTCTGAGGAG<br>GACCTGGTCACCATCAGCAT | mZbp1 | TCAAAGGGTGAAGTCATGGA<br>GTGGAGTGGCTTCAGAGCTT |
| mIfit3 | TTCCCAGCAGCACAGAAAC<br>AAATTCCAGGTGAAATGGCA | m.mtATP6 | CCTTCCACAAGGAACTCCAATTTCAC<br>CTAGAGTAGCTCCTCCGATTAGGTG |
| mIfna1 | GAGAAGAAACACAGCCCCTG<br>TCAGTCTTCCCAGCACATTG | m.mtCO3 | GACGTAATTCGTGAAGGAACCTACC<br>GATAGAACGCTCAGAAGAATCCTGC |
| mIfna4 | CTTTCCTCATGATCCTGGTAATGAT<br>AATCCAAAATCCTTCCTGTCCTTC | m.mtCytb | GCTTTCCACTTCATCTTACCATTTA<br>TGTTGGGTTGTTTGATCCG |
| mIfna5 | GACTCATCTGCTGCATGGAA<br>TGTTGCATCACACAGGCTTT | m.mtDLoop1 | AATCTACCATCCTCCGTGAAACC<br>TCAGTTTAGCTACCCCCAAGTTTAA |
| mIfnb1 | CCCTATGGAGATGACGGAGA<br>CCCAGTGCTGGAGAAATTGT | m.mtND6 | TTTAGCATTAAAGCCTTCACC<br>CCAACAAACCACTTAACAAT |
| mIrgm1 | CCAGGAAGGCCACTAACATC<br>TGGTTCCTTCGAATGCCTTA | m.nucTert | CTAGCTCATGTGTCAAGACCCTCTT<br>GCCAGCACGTTTCTCTCGTT |
| mIsg15 | CTAGAGCTAGAGCCTGCAG<br>AGTTAGTCACGGACACCAG | HSV1 ICP27 RNA | TTTCTCCAGTGCTACCTGAAGG<br>TCAACTCGCAGACACGACTCG |
| mMfn1 | ATGGCAGAAACGGTATCTCCA<br>GCCCTCAGTAACAAACTCCAGT | HSV1 UL30 RNA | CGCGCTTGGCGGGTATTAACAT<br>TGGGTGTCCGGCAGAATAAAGC |
| mPolg2 | TGGAAATGTGTCTACGATACAGG<br>GCTGGAAGGAATCGTAGAGGT | VSV-G | CAAGTCAAAATGCCCAAGAGTCACA<br>TTTCCTTGCATTGTTCTACAGATGG |
| mRnf213 | TTTGTACCGTTCCCCCAAT<br>GTTCACTGCCTCCAATTGCT | VSV-M | TATGATCCGAATCAATTAAGATATG<br>GGGACGTTTCCCTGCCATTCCGATG |

**Table 2.**

List of antibodies and dilutions used.

| Name | Company | Catalog number | Dilution |
|---|---|---|---|
| CLPX | Abcam | ab168338 [EP8772] | 1:1,000 |
| IFIT3 | gift from G.Sen at Cleveland Clinic | | 1:10,000 |
| ZBP1 | Adipogen | AG-20B-0010 | 1:1,000 |
| STAT1 | Cell Signaling | 9172S | 1:1,000 |
| STAT2 (D9J7L) | Cell Signaling | 72604 | 1:1,000 |
| cGAS | Cell Signaling | 31659 | 1:1,000 |
| RIG-I | Cell Signaling | 4200S | 1:1,000 |
| IRGM1 | Cell Signaling | 14979 | 1:1,000 |
| MAVS | Cell Signaling | 4983 | 1:1,000 |
| IRF7 (D8V1J) | Cell Signaling | 72073 | 1:1,000 |
| IRF3 (D83B9) | Cell Signaling | 4302 | 1:1,000 |
| αTUBULIN | DSHB | 12G10 | 1:5,000 |
| GFP | DSHB | 8H11 | 1:30 |
| TFAM | Millipore | ABE483 | 1:1,000 |
| ANTI-DNA | Millipore | CBL-186 (AC-30–10) | 1:300 |
| IFITM1 | Proteintech | 60074–1-Ig | 1:5,000 |
| IFIT2 | Proteintech | 12604–1 | 1:1,000 |
| CALNEXIN | Proteintech | 10427–2-AP | 1:1,000 |
| β-ACTIN | Proteintech | 66009–1-Ig | 1:5,000 |
| CLPP | Proteintech | 15698–1 | 1:1,000 |
| GAPDH | Proteintech | 60004–1-LG | 1:5,000 |
| Histone 3 (H3) | ProteinTech | 17168–1-AP | 1:5,000 |
| HSP60 | Santa Cruz | sc-1052 | 1:5,000 |
| mt-COI | ThermoFisher | 459600 (ID6E1A8) | 1:1,000 |